**Article** 

https://doi.org/10.1038/s44221-024-00252-3

# Pushing the limits of size selectivity in nanoscale solute separations

Received: 24 November 2023

Accepted: 8 May 2024

Published online: 20 June 2024



Check for updates

Feng Gao<sup>1,2,6</sup>, Wen Chen<sup>1,3,6</sup>, Jamila G. Eatman<sup>1,3</sup>, Ruben Z. Waldman<sup>1,3</sup>. Nestor J. Zaluzec<sup>1,4</sup>, Ruilin Dong<sup>3</sup>, Paul F. Nealey<sup>1,3,5</sup> & Seth B. Darling<sup>1,2,3</sup>

Transport of a spherical solute through a cylindrical pore has been modelled for decades using well-established hindered transport theory, predicting solutes with a size smaller than the pore to be rejected nonetheless because of convective and diffusive hindrance; this rejection mechanism prevents extremely sharp solute separations by a membrane. Whereas the model has been historically verified, solute transport through near-perfect isoporous membranes may finally overcome this limitation. Here encouraging solute rejections are achieved using nanofabricated, defect-free silicon nitride isoporous membranes. The membrane is challenged by a recirculated feed to increase the opportunity for interactions between solutes and the pore array. Results show the membrane completely reject solutes with greater size than the pore size while effectively allowing smaller solutes to permeate through. With effectively increasing the number of interactions, we propose that a steeper size-selective rejection curve may be achieved. With this traditional hurdle overcome, there is new promise for unprecedented membrane separations through judicious process design and extremely tight pore-size distributions.

Membrane technology offers compelling options to address diverse processing challenges<sup>1</sup>. Whereas a range of membranes and associated processes are widely operated, there is a need to develop a deeper understanding of transport through membrane pores to enable more advanced membrane technology to meet growing and emerging challenges<sup>2-4</sup>.

Size-selective separation by pore networks is one of the fundamental pillars of membrane separation<sup>5,6</sup>. It is the working mechanism for many membranes technologies, such as ultrafiltration (UF), in which the membrane pore size is 10 nm and above. Utilizing size exclusion, UF can effectively separate or remove various solutes such as microbes, colloidal particles and natural organic matter. Therefore, UF membranes have found wide applications in decontamination of drinking water, wastewater treatment and membrane bioreactors7. Intuitively, one imagines that solutes with sizes smaller than membrane pores can flow through the membrane whereas solutes with size greater than the membrane pores are rejected. As a membrane contains vast numbers of pores, often with a broad range of sizes, separating solutes with small differences in size can be difficult. As the pore size and its distribution affect solute transport through a membrane, development of membranes with uniform pores, known as isoporous membranes, has attracted long-lasting interest<sup>7-10</sup>. As pointed out in several studies, isoporous systems can offer nanostructured membranes with large porosity, low tortuosity and precise, uniform pore size, which potentially lead collectively to simultaneous high permeability and high selectivity<sup>11-13</sup>.

A variety of materials and techniques have been demonstrated to fabricate isoporous membranes <sup>14–20</sup>. Membranes fabricated using block copolymers serve as viable isoporous membranes or templates, which have been extensively characterized for their nanostructures and solute separation performance  $^{9,17,21,22}$ . As the block copolymer can self assemble into regular and periodic nanostructures (for example,

Advanced Materials for Energy-Water Systems (AMEWS) EFRC, Argonne National Laboratory, Lemont, IL, USA. Chemical Sciences and Engineering Division, Argonne National Laboratory, Lemont, IL, USA. 3 Pritzker School of Molecular Engineering, The University of Chicago, Chicago, IL, USA. <sup>4</sup>Photon Sciences Directorate, Argonne National Laboratory, Lemont, IL, USA. <sup>5</sup>Materials Science Division, Argonne National Laboratory, Lemont, IL, USA. <sup>6</sup>These authors contributed equally: Feng Gao, Wen Chen. ⊠e-mail: darling@anl.gov

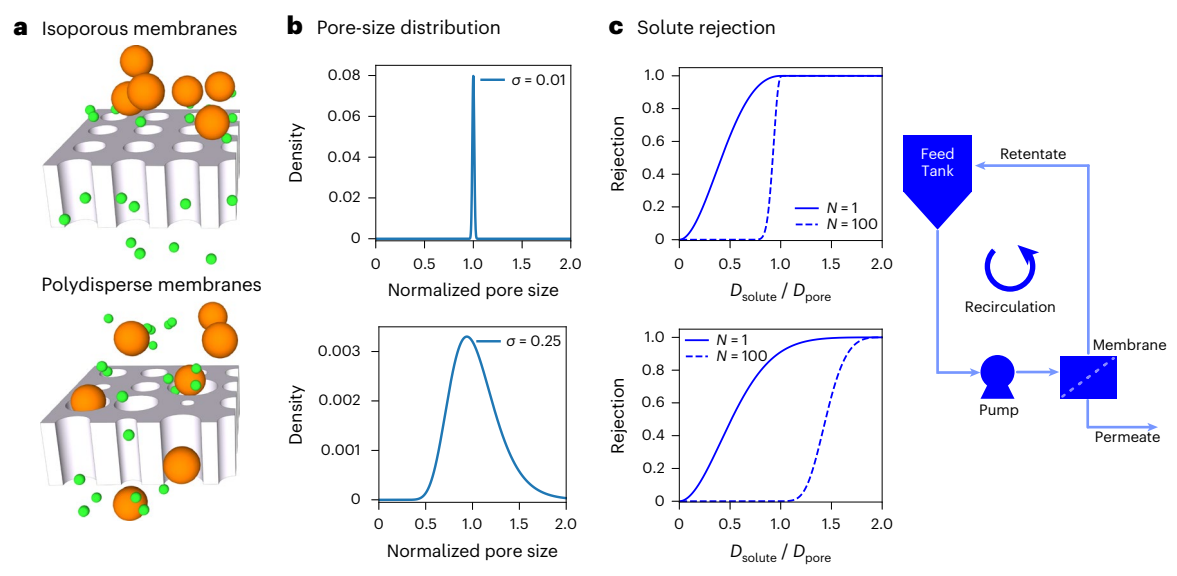


**Fig. 1**| **Solute rejection of ideal isoporous membranes and polydisperse membranes. a**, Schematics of an isoporous membrane and a polydisperse membrane. **b**, Pore-size distribution of both membranes follows a log-normal distribution where the mean pore size is held as a constant. The isoporous membrane has pore-size variance ( $\sigma$ ) of 0.01, whereas the polydisperse membrane has variance of 0.25. **c**, A size-selective rejection vs  $D_{\text{solute}}/D_{\text{pore}}$  curve takes different shapes based on the membrane pore-size distribution.  $D_{\text{solute}}$  is the

solute diameter and  $D_{\rm pore}$  is the mean pore diameter of an isoporous membrane or a polydisperse membrane. Ideally, a sharp, step-function-like rejection curve (dashed curve, top) is expected as recirculated solutes encounter pore entrances of a perfect isoporous membrane after a large number of interactions. In contrast, a soft, sigmoid rejection curve (solid curve) is expected as recirculated solutes interact with pores of varying size on a typical polydisperse membrane.

cylinders, gyroid, lamellae), isoporous membranes are fabricated following any of a number of different processing techniques (for example, selective etching or selective swelling of self-assembled block copolymer, self assembly and non-solvent induced phase separation (SNIPS)). In particular, SNIPS membranes have an asymmetric architecture with a thin, isoporous layer that gradually transitions into a thicker and more porous substructure, enabling a robust platform to investigate solute transport under applied pressure<sup>23-29</sup>. Separation characterization of the membrane is typically operated under a low transmembrane pressure where the membrane is housed within a filtration device. A SNIPS membrane containing pores with near monodisperse diameter have been fabricated using a triblock terpolymer, poly(isoprene-b-styrene-b-4-vinylpyridine)<sup>30</sup>. Characterizing the membrane by filtrating poly(ethylene oxide) solute with various hydrodynamic sizes, the authors showed good agreement between experimental solute rejection and rejections predicted by hindered transport theory. Detailed introduction of hindered transport theory is presented in the next section, 'Theory for size-exclusion membranes'. A comprehensive summary of solute rejection using various block copolymer membranes fabricated by SNIPS, selective etching and swelling methods have been outlined in a recent review<sup>7</sup>. The rejection profiles reported therein are scattered around the theoretical hindered transport curve, indicating a close match between the SNIPS membrane structure and performance of an ideal isoporous membrane predicted by the theory. With these materials, however, one might anticipate that such idealized membranes could offer an extremely sharp rejection curve, where most solutes smaller than the (uniform) pores are transported through the membrane and all those larger are rejected. However, despite decades of studies, solute rejection by a UF membrane still stubbornly follows the prediction of the hindered transport model, which is far from an ideal 'step function' rejection.

In this study, we explore what factors are limiting the sharpness of the rejection curve and attempt to push closer to the step function ideal. Our approach is based on two perspectives: (1) precisely fabricated isoporous membranes using block copolymer self assembly and a series of nanofabrication techniques; (2) carefully operated filtration

experiments and solute analysis. One key hypothesis is that the number of interactions between the solutes and the membrane influences the rejection. That is, solutes with a size smaller than the membrane pore size will *eventually* permeate through the membrane *if* the same solute can interact with the membrane multiple times via recirculation. If this hypothesis is accurate, the rejection curve will evolve with increasing the number of interactions, and a sharp curve approaching a step function may be achieved using an isoporous membranes in the limit of an infinite number of interactions. It should be noted that a typical polydisperse membrane, in contrast, will always struggle to deliver a sharp rejection curve (Fig. 1).

#### Theory for size-exclusion membranes

A solute molecule that is at least several times larger than a solvent molecule can be viewed as a Brownian particle that experiences hydrodynamic resistance to its motion. For a spherical solute, this phenomenon is described by the Stokes-Einstein equation (Supplementary Equation (1)) where the diffusivity of such a particle in an unbounded liquid equals the thermal fluctuation energy divided by the drag coefficient<sup>31</sup>. As the space surrounding the solute becomes constrained (for example, a solute inside a fine pore), the friction coefficient will exceed its value in an unbounded solution, leading to reduced mobility of the solutes inside the pore. Hindered transport theory has provided the basis of selectivity of size-exclusion membranes<sup>31,32</sup>. The theory provides a fundamental description of spherical solutes transporting through cylindrical pores under the effect of diffusion and convection. It depicts a hindered process through a capillary—a process that produces separations much less precise than the simple intuitive picture outlined above.

With hindered transport theory, the pore length is assumed to be considerably larger than its radius, leading to a fully developed flow inside the pore at steady state. The flux of the solute within the pore can be calculated, and it is influenced by diffusion, convection or both, depending on the Péclet number (Pe). Solute transport is dominated by diffusion when Pe  $\ll 1$  and by convection when Pe  $\gg 1$ . On the basis of the theory, solute sieving coefficient (S) is calculated by comparing

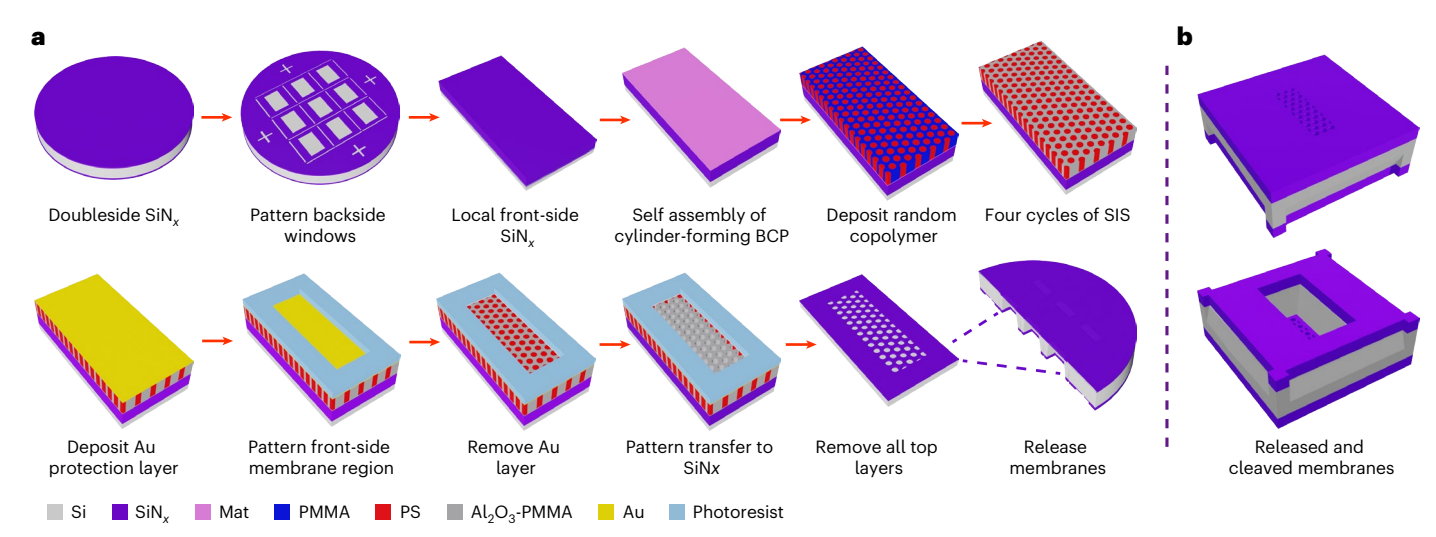


**Fig. 2** | **Fabrication of silicon nitride isoporous membranes. a**, Nanofabrication processes of  $SiN_x$  isoporous membranes templated from cylinder-forming polystyrene-*block*-poly(methyl methacrylate) (PS-*b*-PMMA) block copolymer (BCP), while using sequential infiltration synthesis (SIS) to enhance its etching resistance. Random copolymer (Mat) is used to guide the perpendicular cylinder

geometry.  $\mathbf{b}$ , Front-side (permeate side) and backside (feed side) view of a single  $\mathrm{SiN}_x$  membrane that has been released and cleaved from the wafer. Note the schematic was drawn to highlight details of the nanofabrication process, and the depicted dimensions of the wafer, the membrane window and the individual pores are not at the same scale.

the solute concentration through the pore to that of the solute at the pore entrance. Rejection coefficient (R) of the solute is difference between unity and S. As a function of the ratio between the solute size and pore size (that is,  $\lambda = D_{\rm solute}/D_{\rm pore}$ ), R can be used quantify the membrane's ability to either retain or allow solute passage. An R value of 0 signifies that the solute can freely pass through the membrane whereas an R value of 1 indicates the solute passage is completely blocked. Intermediate values correspond to hindered transport, whereby larger solutes transport more slowly than smaller ones, producing correspondingly lower solute fluxes in the permeate.

Equation (1) below represents a widely applied hindered transport model, which is based on convective flow of rigid spherical particles (diameter  $D_{\text{solute}}$ ) through cylindrical pores (diameter  $D_{\text{pore}}$ )<sup>32</sup>.

$$R = 1 - \left( (1 - \lambda)^{2} \left( 2 - (1 - \lambda)^{2} \right) \left( \exp\left( -0.7146\lambda^{2} \right) \right) \right) \tag{1}$$

To provide context of equation (1), the exponential coefficient term was obtained by a least-squire fit of a  $\lambda$ -based function on the values of drag coefficients<sup>32</sup>,  $(1-\lambda)^2$  is the partition coefficient, which indicates the fraction of the cross-section area of the pore that is accessible to the centre of the spherical solute, and  $(2-(1-\lambda)^2)$ 

accounts for the fully developed, parabolic velocity profile in the pore. According to the theory, R increases nonlinearly (sigmoid) with increasing ratio of the solute size to pore size. Solutes are partially 'rejected' (that is, hindered) when  $\lambda$  is less than 1 ( $D_{\text{solute}} < D_{\text{pore}}$ ) and completely rejected when  $\lambda$  is equal to or greater than 1 ( $D_{\text{solute}} \ge D_{\text{pore}}$ ).

Dictated by hindered transport theory, rejection of a solute with  $\lambda$  less than 1 will always yield R ranging between 0 and 1. This can be attributed to the fact that the theory only models intrapore solute transport. The validity of hindered transport theory has been repeatedly established in this context and is equally applicable to the current study. However, a size-selective separation process also reflects the interaction between a solute and a pore at the pore entrance. In an ideal scenario where the pore is not blocked (for example, fouling) and sufficient feed water is supplied, we postulate that a solute with a size smaller than the pore size will permeate through the membrane when it has an infinite number of attempts to interact with the pore, whereas solutes with a size greater than the pore size will consistently

be rejected. The rates of transport through the pores once the solutes are inside them (that is, hindered transport theory) would no longer limit the ability of the membrane to perform a separation, rather, only the pore-size distribution would govern it. Using a perfect isoporous membrane, this ideal scenario would lead to a sharp, step-like rejection profile.

No real process can achieve an infinite number of solute–pore interactions, but as the opportunities for such interactions increase, the rejection profile should evolve from one fit well by traditional hindered transport theory to a sharper, more precise separation. A simple mathematical representation for the rejection profile of such a process  $(R_N)$  can be built from the traditional R from hindered transport theory, raising it to a power to effectively increase the (size-dependent) concentration of solutes within the pores:

$$R_N = R^N \tag{2}$$

Because the actual number of attempts for an average solute is difficult to extract experimentally, we denote N as a process-based variable that scales proportionally with the number of attempts. A plot of  $R_N$  is shown in Fig. 1 for both a polydisperse membrane and an isoporous membrane.

# Fabrication of silicon nitride isoporous membranes

An illustration of the process used to fabricate block copolymer (BCP)-templated silicon nitride (SiN $_x$ ) membranes is shown in Fig. 2. A Si wafer coated on both sides with 100-nm SiN $_x$  was first patterned to demarcate eventual backside windows. The size of the backside window was designed to expose a 2.5 × 0.7 mm $^2$  membrane region on the front side  $^{33,34}$ .

The formation of the nanoporous template is obtained from self assembly of a cylinder-forming polystyrene-*block*-poly(methyl methacrylate) BCP (PS-*b*-PMMA) on a cross-linked poly(styrene-*co*-methyl methacrylate-*co*-glycidyl methacrylate) random copolymer layer (Supplementary Fig. 1). A sequential infiltration synthesis (SIS) $^{35,36}$  process was applied to convert the PMMA matrix to aluminium oxide-PMMA (Al $_2$ O $_3$ -PMMA) without modifying the structure of the PS cylinders. The SIS-modified structure maintained the same pitch ( $L_0$ ) as the original BCP, and the (unreacted) cylinder diameter was determined by the

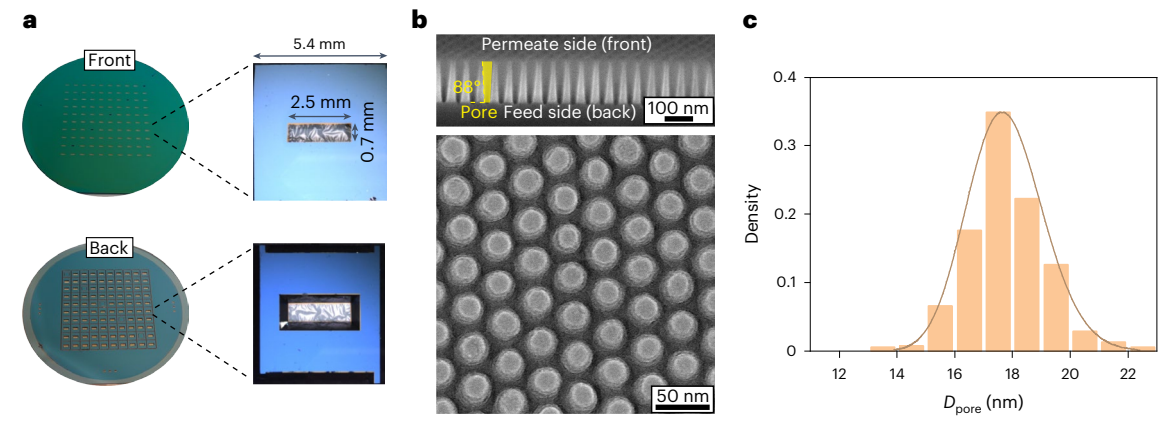


**Fig. 3** | **Pore-size distribution of silicon nitride isoporous membranes. a**, One-hundred chips each with a rectangle membrane window
(2.5 mm × 0.7 mm) are produced on a 4-inch wafer. **b**, Cross-sectional and plane view of silicon nitride isoporous membranes. The cross-sectional image was obtained using SEM and the plane view was obtained using TEM. Each pore has a conical shape with a smaller diameter on the back (feed) side and a larger diameter on the front (permeate). The nanofabricated silicon nitride membranes

produced in one wafer and across different wafers have a narrow pore-size distribution across varying scales as shown in Supplementary Fig. 4. **c**, Statistical analysis of the feed-side pore-size distribution based on ten TEM images of different scanned areas (that is, boundary and centre) on a single membrane. The distribution of pores is fitted using a log-normal distribution (curves), which indicates a mean pore diameter of 17.8 nm ( $\mu$  = 2.89) with a standard deviation of 1.3 nm ( $\sigma$  = 0.07).

number of SIS cycles<sup>22</sup> (Supplementary Fig. 2). Next, a 20 nm gold (Au) layer was deposited on the SIS thin film to apply photolithography to create defined membrane regions while aligning with the backside windows. Gold etchant exposed underneath the Al<sub>2</sub>O<sub>3</sub> nanostructure. Oxygen plasma then selectively removed the PS cylinders. Trifluoromethane/oxygen-based plasma was adopted to transfer the nanoporous Al<sub>2</sub>O<sub>3</sub> etch mask into the underlying SiN<sub>x</sub>. The selected etch condition achieved a sharp sidewall angle (-88°), as shown in Fig. 3b and Supplementary Fig. 3. As the sidewall is not perfectly perpendicular to the membrane surface, conical pores were produced with slightly smaller openings on the backside and larger openings on the front side. To correlate nomenclature with filtration experiments in the next section, we will use 'feed side' and 'permeate side' to refer to backside and front side, respectively. Membranes of different mean pore size can be obtained by developing different etching conditions. Upon etch completion and further removal of process residuals, a 4-inch SiN, wafer accommodating 100 pieces of  $5.4 \times 5.4$  mm<sup>2</sup> membranes with PMMA protection layer on top is shown in Fig. 3a.

Pore-size distribution of membranes from different etching conditions was analysed using scanning electron microscopy (SEM) and transmission electron microscopy (TEM). Accurate pore-size control and measurement is essential for interpreting solute transport at the nanoscale. Pore-size analysis based on SEM images of membrane fabricated from one single wafer is shown in Supplementary Fig. 4. We note that SEM imaging of the membrane surface has the challenge of arbitrary definition of the pore edge, introducing uncertainty into the characterization, so the scanning transmission electron microscopy (STEM) mode of TEM was selected to precisely determine the membrane pore-size distribution (Fig. 3b). The focus depth was on the feed-side pore edge (small pore ends) such that a clear image of the edges can be obtained, and ImageJ was used to manually draw ellipses covering each pore area. The collected ellipse size information from > 300 pores per membrane was used to represent the membrane pore-size distribution. Histograms of each membrane are plotted in Fig. 3c, while pore-size data were fitted with a log-normal distribution to obtain mean pore size  $\mu$  and variance  $\sigma$ .

### Water permeance and neutral solutes rejection

Water flux through SiN<sub>x</sub> membranes was quantified using a crossflow filtration system described in the Methods section. The flux of water through the membrane was measured at varying transmembrane

pressures (Fig. 4a). Pure water permeance  $^{-965} \, l \, m^{-2} \, h^{-1} psi^{-1}$  was calculated based on the slope of the data. The results were compared to theoretical values predicted by the Hagen–Poiseuille equation while considering the cylindrical pores, with the diameter of the mean pore size 17.8 nm (blue dashed line) and mean pore size with added variance 19.1 nm (green dashed line), perpendicularly aligned to the membrane surface  $^{12}$ . To enable flow of water through a  $SiN_x$  membrane, the membrane was first air plasma cleaned and wetted using isopropanol. Measured permeance changed substantially in the initial hours due to the evolution of surface wettability towards less hydrophilic. The permeability experiment was therefore carried out after stabilizing flux for 24 h with increasing and decreasing pressure applied across the membrane. The measured permeance lies between the two theoretical predictions and exhibits a linear relationship between flux and applied pressure.

The SiN<sub>x</sub> isoporous membranes were characterized using a mixed dextran solution  $(1 g l^{-1} M_n \sim 40,000 g mol^{-1})$  and  $2 g l^{-1}$  $M_n \sim 150,000 \,\mathrm{g} \,\mathrm{mol}^{-1}$ ) to intentionally broaden the molecular weight distribution of the feed solution and ensure the presence of solutes of sizes spanning a range from much smaller to much larger than the pore diameter. Dextran was selected as it is a neutral, inert polymer with  $well-correlated \,molecular\,weight\,with\,hydrodynamic\,size^{37-39}.\,A\,series$ of permeate and retentate samples were collected during long-term, recirculating filtration experiments. By sampling at different points in time, it is possible to identify if the rejection behaviour is static or evolving, as the feed stream has increasing opportunities to interact with the membrane. The concentration and molecular weight distribution of the sample were analysed using a gel permeation chromatography (GPC) system as described in the Methods. Characteristic concentration (g l<sup>-1</sup> and mol l<sup>-1</sup>) vs molecular weight distribution plots of permeate and retentate samples (cumulative filtration time = 187.3 h) is presented in Fig. 4b and Supplementary Fig. 13, whereas data from all permeate and retentate samples are included in Supplementary Fig. 6. A broad molecular weight distribution was detected in the retentate, but the permeate exhibited a single, narrow peak covering the low-molecular-weight range. Using concentrations of permeate, retentate and initial feed samples, rejection curves of varying cumulative filtration time are calculated based on equation (4) and presented in Fig. 4c. Actual rejections were reported to account for the effect of concentration polarization<sup>40</sup>. The hydrodynamic diameter of dextran molecules was calculated based on their molecular weight

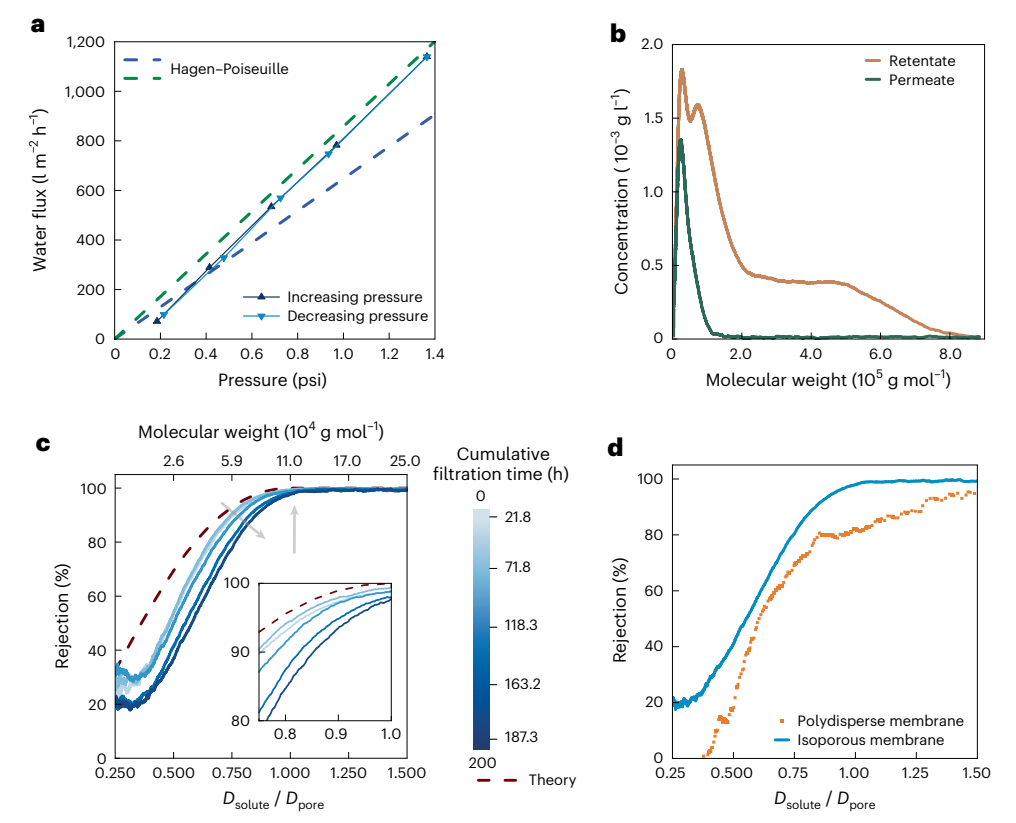


Fig. 4 | Water and dextran transport through silicon nitride membranes. a, Water flux through silicon nitride membranes vs applied pressure (measured twice, first increasing pressure then decreasing through the range). The permeance of the membrane was calculated from the slope of the data. The water fluxes are compared with the Hagen–Poiseuille equation (dashed lines) with a pore diameter of 17.8 nm and 19.1 nm. b, Characteristic molecular weight distribution of dextran in retentate and permeate samples at the final stage of the long-term filtration experiment (cumulative filtration time = 187.3 h). Total

concentration of each sample and molecular weight distribution information is extracted from GPC.  $\mathbf{c}$ , Dextran rejection curves calculated at varying cumulative filtration times are compared to the hindered transport model.  $\mathbf{d}$ , Rejection of dextran using the  $\mathrm{SiN}_x$  membrane is compared to that of a PAN UF membrane. The  $D_{\mathrm{pore}}$  value of the  $\mathrm{SiN}_x$  membrane and the PAN membrane are based on the mean pore size of the corresponding pore-size distribution for each membrane where it is 17.8 nm for  $\mathrm{SiN}_x$  and 14.6 nm for PAN (Supplementary Fig. 5).

and is shown in the supporting information; a constant mean pore diameter 17.8 nm was used based on the TEM pore-size analysis. The rejection data when  $\lambda$  ( $D_{\rm solute}/D_{\rm pore}$ ) < 0.25 were discarded since the data were noisy and unphysical (negative). The noise was caused by an artefact in the GPC signal—a negative peak starting around 25 min was observed in the refractive index. This negative peak affected data of low-molecular-weight dextran (corresponding to  $D_{\rm solute}/D_{\rm pore}$  < 0.25), which were eluted at times approaching the 25 min threshold. The origin of the negative peak was attributed to (1) the phosphate-buffered saline (PBS) solution in which dextran was dissolved had a lower refractive index than the mobile phase (1  $\times$  PBS solution) of the GPC and (2) dissolved gas or small concentration difference exist between the two PBS solutions.

As the cumulative filtration time extended, it was observed that the rejection was not static, rather, it decreased for each  $\lambda$  when  $\lambda$  < 1, and the rejections merged to near 100% as  $\lambda$  approached 1. This time evolution of the rejection curve is a strong indication that the solutes in the feed are experiencing multiple opportunities to interact with the membrane pores as the feed solution recirculates. In general, the rejection curve sharpened with increasing cumulative filtration time, with the point at which rejection deviates below 100% remaining nearly constant at  $D_{\text{solute}}/D_{\text{pore}}$  -1. Such changes are highlighted in an inset in Fig. 4c. This result is a hallmark predicted here for an isoporous membrane where the solute number of interactions is increasing, as shown schematically in Fig. 1. At raditional rejection curve derived from hindered transport theory is also plotted in Fig. 4c for comparison. Comparing rejection curves of the experimental data with the hindered

transport model, the  $SiN_x$  isoporous membrane showed rejection curves with considerably steeper slope when  $\lambda < 1$ .

The experimental rejection curves in Fig. 4c are intriguing for several reasons. On one hand, the curves do not follow the theoretical prediction when  $\lambda$  is less than 1, and the rejection curve sharpens over filtration time. This behaviour suggests a greater value of selectivity between similar-sized neutral solutes in comparison to hindered transport theory, which was developed based on an isoporous membrane. On the other hand, the experimental rejection also does not achieve an ideal 'step function' rejection, which would exhibit no rejection until  $\lambda$  = 1 and then complete rejection above this critical value. Several hypotheses are developed to explain the aforementioned rejection curve features.

To explain the deviation between the hindered transport rejection curve and the experimental curves, a key hypothesis focuses on the concept of the number of interactions between the solutes and the membrane. That is, solutes with size smaller than the membrane pore size will *eventually* permeate through the membrane if the same solute can interact with the membrane multiple times via recirculation. Such a parameter is challenging to measure directly in experiment, and to our best knowledge, the number of interactions has not been explored in the membrane community to interpret rejection behaviour. Here we assumed the number of interactions equals to one for all hindered transport model-based rejection curves, as has been the practice in the membrane science field. The rejection curve becomes closer to a step function by raising R to higher powers (for example, the 100th power, representing N=100 where N is a process-based variable that

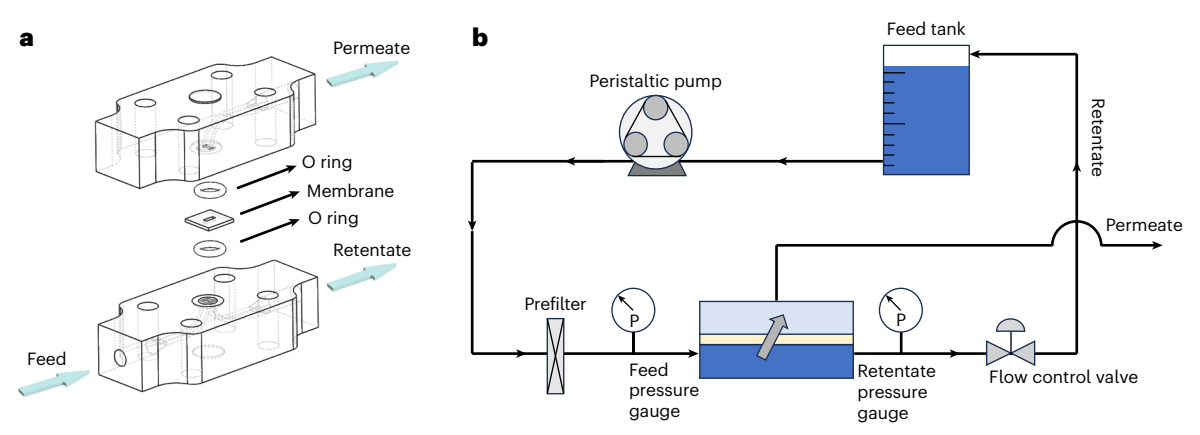


Fig. 5 | A 3D-printed crossflow device and filtration system are assembled to characterize water and solute transport. a, Schematic of a 3D-printed crossflow filtration device used to house silicon nitride membranes. b, A flow

diagram of a crossflow filtration system enabling solute and solvent to be recirculated within the system. Note that the back side (small pore ends) of the membrane always face the feed solution.

scales proportionally with the number of attempt; Fig. 1). The filtration experiment in the present study was executed for -200 h to capture potential evolution of rejection curves; during this period of time, the feed volume was recirculated more than 900 times under a constant recirculation flow rate (7 ml min<sup>-1</sup>). Moreover, the custom flow cell used in this study has structural features intended to induce an increased vertical component of the fluid flow to impinge more solutes onto the membrane surface during a given pass of the fluid.

As shown in Fig. 4c, the rejection curves became steeper as the cumulative filtration time increased. Here the slope of each rejection curve is calculated and shown in Supplementary Fig. 7a. The slope values are also plotted against characteristic values of  $\lambda$  in Supplementary Fig. 7b. It is clear that the slope increased with increasing cumulative filtration time, especially when  $\lambda > 0.5$ . Rejection change between the initial (cumulative filtration time = 21.8 h) and the final (cumulative filtration time = 187.3 h) stage of the filtration for several characteristic values of  $\lambda$  are shown on Supplementary Fig. 8a. ON the basis of the number of interactions hypothesis, dextran solutes should be able to interact with the SiN<sub>x</sub> isoporous membrane more than once when they are recirculated within a closed system with extended filtration time. The hypothesis is derived using a previously developed analytical model that predicts solute rejection of isoporous membranes and polydisperse membranes<sup>12</sup>. Similar rejection variation was observed between the model (using a perfect isoporous membrane at N=1 and 2) and the experiments obtained using the SiN, isoporous membrane (Supplementary Fig. 8b,d). Solutes that are much smaller than the pores of the isoporous membrane (that is,  $\lambda$  < 0.9), even if they are hindered and rejected on a given attempt, eventually can transport through the membrane given a larger number of interactions. Solutes with diameters approaching the pore size of the isoporous membrane (that is,  $\lambda > 0.9$ ) are hindered to a greater extent comparing to the small solutes but are nonetheless able to transport through the pores when the interaction number is sufficiently high. Solutes that are larger than the pores of the isoporous membrane (that is,  $\lambda > 1.1$ ) are universally rejected by the membrane due to steric hindrance despite multiple chances provided via recirculation. The aforementioned interpretation aligns with the observed evolution of rejection presented in Supplementary Fig. 8d, where rejection variation is plotted as a function of  $\lambda$ .

It is clear that the experimental rejection curves do not follow the traditional convection-dominated hindered transport model. As the Pe of solutes was near 1 due to the small transmembrane pressures, hindered transport rejection curves that account for both convection and diffusion are plotted in Supplementary Fig. 9 along with the experimental rejection data. Whereas such a transport model more accurately captures the physics involved in the experiment (and predicts a somewhat sharper rejection curve), it still does not predict the observed time evolution of rejection *unless the number of interactions phenomenon is also considered*.

The separation capability of these isoporous membranes is further highlighted when comparing with commercial UF membranes with similar mean pore size but larger pore-size distribution. Using the same feed solution, dextran rejection by a commercial polyacrylonitrile membrane (PY, PAN 100 kDa, Synder Filtration) with pore size of 14.6  $\pm$  4.3 nm was tested and compared with the SiN $_x$  membrane (Figs. 4d and 5). A soft rejection curve was obtained where the rejection increased slowly over a wide range of  $\lambda$ . Complete rejection (R = 100%) was not reached until  $\lambda$  ~ 1.5. The soft rejection curve of the polyacrylonitrile ultrafiltration (PAN UF) membrane can be attributed to the broad distribution of pore size of the commercial membrane. In stark contrast, the SiN $_x$  membrane functioned much more effectively with a steep rejection change from 0 – 100% when  $\lambda$  is less than 1.

Therefore, the observation of rejection sharper than predicted by convective hindered transport coupled with time-evolving rejection suggests that the number of interactions is both contributing to the separation performance and a possible route to enhance process design in separations. There remains a question, however, of why the ideal step function rejection curve is not obtained in this experiment. Hypotheses to explain the gap between the experimental curves and the ideal sharp cut-off might involve solute–solute interactions, solute–membrane interactions beyond size exclusion and insufficient number of interactions between solutes and membrane.

Potential attractive solute-solute interaction resulting in polymer aggregation exceeding the pore size could lead to the obtained experimental curve with large rejections when  $\lambda < 1$ . Dynamic light scattering measurement of the feed dextran solution was executed to analyse the dextran size distribution in a non-destructive manner. The dextran size distribution in Supplementary Fig. 10 indicated that there were no notable aggregates with size larger than the pore size. Additionally, calculation showed the polymer overlap concentration (>45 g l<sup>-1</sup>) was greater than the feed concentration of the experiment, 3 g l<sup>-1</sup>. These facts suggest the feed was, in fact, a dilute solution with no attractive interactions between the solutes influencing effective solute size. Potential solute-membrane interactions, such as adsorption, could also contribute to the enhanced rejection for intermediate solute sizes. We observed decreased water flux during the long-term filtration experiments, in which the flux typically dropped ~80% by the end of the filtration. Considering that the solute size cut-off (rejection = 100%) remained constant throughout the cumulative filtration time, it is conceivable that some solutes were adsorbed to the membrane/pore surface, leading to fouling. Whereas a full cake layer was not formed

given that the rejection of small solutes remained low throughout the long-term filtration, solute adsorption could reduce transport of small dextran species through the membrane and result in anomalously large rejection by spatially restricting some pores. This phenomenon cannot be discounted in this experiment, and future studies will be aimed at elucidating the solute–membrane interactions and their potential role in rejection.

Perhaps the most likely explanation for the less-than-ideal sharpness of the rejection curve, however, comes back to the number of interactions concept. We suspect the effective number of interactions between dextran solutes and the membrane during the long-term filtration, whereas greater than in a traditional separation process, was still insufficient to allow for complete permeation of solutes smaller than the pores. This hypothesis is supported by simulating steady-state bulk flow profiles within the feed compartment considering the relatively high membrane permeability and small transmembrane pressure. This simulation showed that flow streamlines are largely oriented parallel to the membrane surface within the feed channel (Supplementary Fig. 11). Meanwhile, the calculated Stokes number describing the behaviour of particles suspended in fluid flow is considerably smaller than one<sup>41,42</sup>, indicating a substantial fraction of the dextran followed the bulk flow streamlines at steady state and therefore did not interact frequently with the membrane. If this hypothesis is correct, then processes designed to further enhance the amount of interaction between the solutes and the membrane surface would be likely to achieve even more precise separations than those observed in this study.

#### Conclusion

We demonstrated ultrahigh-resolution neutral solute separation performance using custom-fabricated  $\mathrm{SiN}_x$  isoporous membranes with pore size of  $17.8 \pm 1.3$  nm. Whereas separation within this pore-size regime is traditionally described by hindered transport theory, these results challenge the theory with a notably steeper rejection curve. Governing mechanism(s) that underlie this superior separation performance remain a focus of ongoing studies, but there are strong indications that the solutes are undergoing multiple interactions with the membrane's pore array. Further exploration using intentionally, and systematically, non-isoporous membranes will represent a powerful platform for deciphering complex phenomena coupling pore-size distribution and separation performance. It is apparent that nearly perfect membranes can reveal new insights into longstanding theories of nanoscale solute transport and offer pathways to deliver more effective separations.

#### **Methods**

## Materials

Silicon wafers (4 inch, N-type, (100) orientation) coated with low-stress silicon nitride were purchased from Pure Wafer. The wafers were double-side polished, and the nitride was deposited using low-pressure chemical vapour deposition with a stress of less than  $250 \pm 50$  MPa tensile. All wafers in this study had a thickness of 500-535 μm, and the nitride thickness was 100 nm. AZ MiR 703 photoresist and AZ 300 MIF developer were purchased from EMD Performance Materials Corp. Cylinder-forming poly(styrene-*block*-methyl methacrylate) (PS-*b*-PMMA) ( $M_n = 20.5 - b - 59.0 \text{ kg mol}^{-1}$ , denoted as C2059, polydispersity index (PDI) = 1.04,  $L_0$  = 35 nm) and poly(ethylene oxide)  $(M_n = 30,000, 35,000, 39,000, 55,000, 58,000, 81,000, 95,000$  and 150,000 g mol<sup>-1</sup>) used for filtration tests were purchased from Polymer Source Inc. Poly(styrene-co-methyl methacrylate-co-glycidyl methacrylate) random copolymer containing 4 mol% of glycidyl methacrylate and 60 mol% of styrene (denoted as 60 S) was synthesized by reversible addition-fragmentation chain transfer polymerization. Potassium hydroxide pellets (ACS reagent, 85%) were purchased from Oakwood Products Inc. Gold etchant was purchased from Transene Electronic Chemicals and used as received. ProTEK B3 Primer was purchased from Brewer Science Inc. and used as received, and 495k PMMA was purchased from EM RESIST LTD and used as received. Dextran ( $M_n = 40,000 \, \mathrm{g \ mol^{-1}}$  and 150,000 g mol<sup>-1</sup>) were purchased from TCI chemical and Thermo Scientific, respectively. All solvents were purchased from Sigma Aldrich and used as received.

#### SiN<sub>r</sub> membrane sample preparation

AZ MIR 703 was spin coated on the backside of a double-sided  $\mathrm{SiN}_x$  wafer at 3,500 r.p.m. and baked at 95 °C for 1 min. The resist was then patterned in a Heidelberg MLA150 direct write lithographer to define windows and alignment marks. The patterned wafer was developed in AZ 300 MIF developer for 60 s and rinsed with water. The exposed  $\mathrm{SiN}_x$  was then etched and removed with  $\mathrm{CHF}_3/\mathrm{O}_2$  plasma in a PlasmaTherm RIE instrument. The remaining resist was removed with *N*-Methylpyrrolidone (NMP) at 80 °C. The wafer was further cleaned in a nanostrip solution at 80 °C for 40 min to remove contamination on the front side and then rinsed with water.

The front side of SiN<sub>x</sub> was then coated with an aluminium oxide (AlO<sub>x</sub>) cylindrical-pore nanostructure templated from a C2059 BCP thin film according to the following process. After creating backside windows, the SiN<sub>x</sub> wafer was coated with the 60 S mat, which was designed to be energetically neutral to both blocks of C2059. To prepare the mat, a 0.3 wt% solution of 60 S in toluene was spin coated to a thickness of ~11 nm. Film thicknesses were measured by ellipsometry using a Cauchy model. The mat was cross linked by annealing on a hot plate in an N<sub>2</sub> glovebox for 20 min at 235 °C. Then, excess unreacted mat was removed by ultrasonication in toluene for 5 min. After annealing and rinsing, the neutral mat thickness decreased slightly to ~9 nm. Subsequently, a filtered 2.2 wt% solution of C2059 in toluene was spin coated directly onto the wafer to a target film thickness of 91 nm, which was thermally annealed at 270 °C for 2 h on a hot plate in a N<sub>2</sub> glovebox. The BCP film was converted into AlO<sub>x</sub> nanostructures using sequential infiltration synthesis (SIS), as published in a previous study 22,42.

Next, the cylindrical AlO<sub>x</sub> structure was transferred into SiN<sub>x</sub>. Twenty nm gold was deposited on the AlO<sub>x</sub> layer using an electron-beam evaporator. AZ MIR 703 resist was spin coated onto the gold layer and baked at 95 °C for 1 min. The resist was then patterned in a direct write lithographer to define the membrane regions. After membrane regions were developed, a 15 s O<sub>2</sub> plasma was applied to remove the residual resist. Then, the SiN, wafer was baked in an oven at 120 °C for 1 h. After 1h, the SiN<sub>x</sub> wafer was soaked in a gold etchant for 30 s to expose the AlO<sub>x</sub> structure under the gold layer. Next, the entire SiN<sub>x</sub> wafer was etched by O<sub>2</sub> plasma for 10 mins in a PlasmaTherm RIE to selectively remove the PS cylinders. Next, a CHF<sub>3</sub>-based plasma etch was used to etch holes into the underlying SiN<sub>x</sub> using the SIS nanostructure as an etch mask. After pattern transfer of the cylindrical geometry to SiN<sub>x</sub>, the wafer was soaked in NMP at 80 °C for 15 mins to remove resist and then gold etchant to remove remaining gold. Eventually, all remaining organic structure was removed with a nanostrip solution at 80 °C for 40 min; the wafer was then rinsed with deionized (DI) water and dried with a N<sub>2</sub> gun.

After fabricating the nanoporous  $SiN_x$ , the wafer was spin coated with filtered ProTEK Primer at 1,500 r.p.m. for 60 s and baked on a hotplate at 205 °C for 1 min. Next, the wafer was spin coated with filtered 495k PMMA at 1,500 r.p.m. and baked on a hotplate at 180 °C for 5 mins. The wafer was placed in a wet etch holder (4 inch TandemTM from AMMT) with the backside with the windows pattern exposed, whereas the front side was sealed off by O rings. The set-up was immersed in 30 wt% KOH solution at 85 °C. When there were no further bubbles coming out from the set-up (-5 hr), the holder was removed from the KOH solution and rinsed with DI water. After the wafer was removed from the holder and dried, the front-side PMMA protection layer was removed by a 15 min  $O_2$  plasma etch.

#### Transmission electron microscopy

Transmission/scanning transmission electron microscopy (TEM/ STEM) and X-ray energy dispersive spectroscopy measurements in this study were conducted using the Argonne PicoProbe Analytical Electron-Optical Beam Line/Microscope<sup>43</sup>. Imaging reported herein was conducted at 300 kV using high angle annular dark field and bright field (BF) STEM and phase contrast BF TEM. During imaging and hyperspectral measurements, electron-beam currents of ~100 pA were typically employed whereas probe sizes and operating modes were varied as appropriate to the spatial resolution required. TEM image and diffraction data were collected on the post column complementary metal oxide semiconductor (CMOS) 4k × 4k camera, whereas STEM images were acquired on both using BF and high angle annular dark field detectors, which were integrated into the microscope. By careful control of operating conditions (electron beam, energy and dose), the pores did not noticeably change under observation, and no substantial hydrocarbon contamination was observed that would affect image measurements. Temporally resolved hyperspectral X-ray energy dispersive spectroscopy was additionally carried out as needed using the Argonne X-ray Perimeter Array Detector and allowed the monitoring of any mass loss due to electron-beam induced sputtering/ radiolysis with negligible effects being observed.

Pore metrology was conducted using ImageJ. To precisely preserve the porous area from the original TEM/STEM data, images were first adjusted for brightness and contrast to enhance the pore edges, then black ellipses were applied manually and adjusted to cover pores to enable identification of a clear edge. The resulting metrological measurements of the ellipses were then processed to yield pore-size analysis.

#### Scanning electron microscopy

Scanning electron microscopy (SEM) images of fabricated  $SiN_x$  membranes were used to extract size distributions from five membranes. The back pattern of a 4 inch  $SiN_x$  wafer was designed to contain five additional membranes without a back etch at fixed locations. Imaging of these supported membranes mitigated drift that would otherwise occur at high magnifications as a result of charging of the sample. To obtain analysable images of the backside pores, the membrane frame was attached on a conductive double-side copper tape such that only the non-porous region contacted directly with the conductive tape and the porous  $2.5 \times 0.7 \text{ mm}^2$  region was suspended. All membranes were imaged directly after being fabricated without coating any conductive materials so as to accurately represent the original size and shape of the pores. All diagnostic images were taken as a 1  $\mu$ m-wide image with a resolution of 1,024  $\times$  1,024 pixels.

Pore metrology was achieved using a custom MATLAB code to not introduce artificial errors. First, a top-down SEM image of nanopores was imported into the MATLAB script and used for 2D image analysis. Next, Otsu's method was applied to perform automatic image thresholding of the imported image excluding the SEM information bar, forming a binary image composed of only black and white. Then, through labelling all detected pores and counting how many pixels are inside each pore, a table of the pore sizes was formed. After deleting incomplete pores at the boundary, the table was imported to OriginLab for further data processing.

#### Water permeance measurement

Adventitious carbon and other surface contaminants influence the hydrophilicity of the fabricated membranes, so a surface treatment is needed to produce reliably and reproducibly hydrophilic pores for subsequent transport studies.  $\mathrm{SiN}_x$  membranes were placed on a metal mesh in a chamber of a plasma cleaner (Harrick basic plasma cleaner, model PDC-32G). Membranes were cleaned under air plasma with 18 W RF power for 20 min before transport tests.

After plasma cleaning,  $SiN_x$  membranes were analysed under an optical microscope to ensure that the membrane window has no

macroscopic defects. A custom 3D-printed crossflow filtration cell (Fig. 5a) was designed to house the  $\mathrm{SiN}_x$  membranes. The porous membrane window was sandwiched between two O rings to seal both sides and isolate the porous region. The  $\mathrm{SiN}_x$  membrane was implemented on the flow cell with the narrower ends of the pores (backside) facing towards the feed side. To begin assembly, the membrane was first wetted with isopropanol alcohol. The channels within the feed and permeate parts of the flow cell were also prefilled with a small volume of isopropanol alcohol. The flow cell, membrane and two O rings were then assembled as indicated in Fig. 5a. The membrane-integrated flow cell was then incorporated into a crossflow filtration system shown in Fig. 5b. A polyethersulfone syringe filter with 0.2  $\mu$ m pore size was implemented before the flow cell to prevent large particles from other parts of the system (for example, tubing) entering and fouling the  $\mathrm{SiN}_x$  membrane.

To begin the water permeability test, the feed tank was filled with ~50 ml of Dl water. The feed water was then recirculated within the system for 20 h to reach a stable water flux. The permeating solution was collected using a scintillation vial and weighed on a balance. The steady-state water flux at each applied pressure was calculated by measuring the mass of the permeate as a function of time. The variation of the water flux over a range of applied pressure from 0.2 to 1.5 psi was used to calculate the hydraulic permeability of the membranes. A transmembrane pressure  $(P_{\text{TMP}})$  was calculated as

$$P_{\text{TMP}} = \frac{P_{\text{f}} + P_{\text{r}}}{2} - P_{\text{p}} \tag{3}$$

where  $P_f$  and  $P_r$  are readings from feed and retentate pressure gauge, respectively.  $P_p$  is the permeate pressure, which is assumed to be the ambient gauge pressure (zero).

#### **Dextran rejection experiment**

A mixed dextran solution was prepared to intentionally broaden the molecular weight distribution (and therefore dextran size distribution) of the feed solution. The feed was prepared by dissolving 1 g l<sup>-1</sup>  $M_n = 40,000 \text{ g mol}^{-1} \text{ dextran and } 2 \text{ g l}^{-1} M_n = 150,000 \text{ g mol}^{-1} \text{ dextran in}$ pH = 7.4 PBS water. To start a rejection test, DI water was flowed through the crossflow system with a SiN, membrane for 20 h. Then, the water within the system was drained, and the system was refilled with the dextran feed solution. A transmembrane pressure of 0.2-0.5 psi was applied. The first 0.5 ml permeating solution was discarded to eliminate the effect of residual water within the permeate tubing on solute concentration, and then a series of permeate and retentate solutions each with 0.5-1.5 ml were collected using scintillation vials at different time intervals. Concentration and molecular weight distribution of each permeate and retentate sample was evaluated using a Toso EcoSEC gel permeation chromatography (GPC) system equipped with a refractive index detector. Molar mass distributions of dextran were determined with respect to calibration standards (PEO) over a broad range of polymer molecular weights (~200-1,000,000 g mol<sup>-1</sup>) using two Tosoh SuperAW columns in series (3,000 and 4,000).

Observed rejection of a solute was calculated using equation (4).

Rejection (%) = 
$$\left(1 - \frac{c_p}{\frac{c_r + c_r}{2}}\right) \times 100$$
 (4)

where  $c_{\rm p}$  and  $c_{\rm r}$  are the solute concentration in the permeate side and the retentate (feed) side of the membrane, respectively.  $c_{\rm f}$  is the solute concentration in the initial feed solution.

Dextran concentration of a specific molecular weight in the permeate and the retentate solutions were obtained by GPC analysis. First, the total area under the curve of each permeate and retentate from the original chromatogram (Supplementary Fig. 6a) was calculated.

The total concentration of each sample was obtained by calibrating with the chromatogram of the initial feed dextran solution with a known  $3\,\mathrm{g}\,\mathrm{l}^{-1}$  concentration. Then, area of each 'thin slice' under a curve in the chromatogram was calculated and converted to concentration. Next, the elution time was converted into an effective dextran molecular weight using the PEO calibration standards. Last, a series of permeate and retentate molecular weight distribution with respect to concentration were obtained and shown in Supplementary Fig. 6b.

The diffusion coefficient of a dextran molecule was calculated based on a well-developed correlation<sup>32</sup>, and the hydrodynamic size of polymers with varying molecular weight were obtained using the Stokes–Einstein equation. Actual rejection coefficient, which accounted for the effect of concentration polarization, was analysed based on the thin film model<sup>5,40</sup>. Additionally, while the filtration experiments were executed with the inline prefilter, the prefilter did not reject the feed dextran solutes, as shown in Supplementary Fig. 12.

# **Data availability**

The data that support the findings of this study are available via Figshare at https://doi.org/10.6084/m9.figshare.24773811.v1 (ref. 44).

#### References

- 1. Sholl, D. S. & Lively, R. P. Seven chemical separations to change the world. *Nature* **532**, 435–437 (2016).
- Gin, D. L. & Noble, R. D. Designing the next generation of chemical separation membranes. Science 332, 674–676 (2011).
- Werber, J. R., Osuji, C. O. & Elimelech, M. Materials for next-generation desalination and water purification membranes. *Nat. Rev. Mater.* 1, 16018 (2016).
- 4. Lee, A., Elam, J. W. & Darling, S. B. Membrane materials for water purification: design, development, and application. *Environ. Sci. Water Res. Technol.* **2**, 17–42 (2016).
- Zeman, L. J. & Zydney, A. L. Microfiltration and ultrafiltration: principles and applications. *Chem. Ing. Tech.* 69, 1479–1479 (1997).
- Baker, R. W. Membrane Technology and Applications (John Wiley & Sons. 2012).
- Hampu, N. et al. Next-generation ultrafiltration membranes enabled by block polymers. ACS Nano 14, 16446–16471 (2020).
- Peinemann, K. V., Abetz, V. & Simon, P. F. W. Asymmetric superstructure formed in a block copolymer via phase separation. Nat. Mater. 6, 992–996 (2007).
- Abetz, V. Isoporous block copolymer membranes. Macromol. Rapid Commun. 36, 10–22 (2015).
- Warkiani, M. E. et al. Isoporous micro/nanoengineered membranes. ACS Nano 7, 1882–1904 (2013).
- Park, H. B. et al. Maximizing the right stuff: the trade-off between membrane permeability and selectivity. Science 356, eaab0530 (2017).
- Waldman, R. Z. et al. Maximizing selectivity: an analysis of isoporous membranes. J. Membr. Sci. 633, 119389 (2021).
- Zhang, Z. et al. Highly selective isoporous block copolymer membranes with tunable polyelectrolyte brushes in soft nanochannels. J. Membr. Sci. 646, 120266 (2022).
- 14. Lei, Y., Cai, W. & Wilde, G. Highly ordered nanostructures with tunable size, shape and properties: a new way to surface nano-patterning using ultra-thin alumina masks. *Progr. Mater. Sci.* **52**, 465–539 (2007).
- Phillip, W. A. et al. Self-assembled block copolymer thin films as water filtration membranes. ACS Appl. Mater. Interfaces 2, 847–853 (2010).
- Mulvenna, R. A. et al. Tunable nanoporous membranes with chemically-tailored pore walls from triblock polymer templates. J. Membr. Sci. 470, 246–256 (2014).

- Nunes, S. P. et al. From micelle supramolecular assemblies in selective solvents to isoporous membranes. *Langmuir* 27, 10184–10190 (2011).
- Zhang, Z. et al. Hybrid organic-inorganic-organic isoporous membranes with tunable pore sizes and functionalities for molecular separation. Adv. Mater. 33, 2105251 (2021).
- Vlassiouk, I. et al. Versatile ultrathin nanoporous silicon nitride membranes. Proc. Natl Acad. Sci. USA 106, 21039–21044 (2009).
- Wright, E. et al. Development of isoporous microslit silicon nitride membranes for sterile filtration applications. *Biotechnol. Bioeng.* 117, 879–885 (2020).
- Sun, W. et al. Surface-active isoporous membranes nondestructively derived from perpendicularly aligned block copolymers for size-selective separation. J. Membr. Sci. 466, 229–237 (2014).
- Zhou, C. et al. Fabrication of nanoporous alumina ultrafiltration membrane with tunable pore size using block copolymer templates. Adv. Funct. Mater. 27, 1701756 (2017).
- 23. Zhu, G.-D. et al. Isoporous membranes with sub-10 nm pores prepared from supramolecular interaction facilitated block copolymer assembly and application for protein separation. *J. Membr. Sci.* **566**, 25–34 (2018).
- 24. Karunakaran, M. et al. Isoporous PS-b-PEO ultrafiltration membranes via self-assembly and water-induced phase separation. *J. Membr. Sci.* **453**, 471–477 (2014).
- 25. Pendergast, M. M. et al. Understanding the structure and performance of self-assembled triblock terpolymer membranes. J. Membr. Sci. **444**, 461–468 (2013).
- 26. Dorin, R. M. et al. Designing block copolymer architectures for targeted membrane performance. *Polymer* **55**, 347–353 (2014).
- Gu, Y. & Wiesner, U. Tailoring pore size of graded mesoporous block copolymer membranes: moving from ultrafiltration toward nanofiltration. *Macromolecules* 48, 6153–6159 (2015).
- 28. Liu, Y. et al. Fabrication of a novel PS4VP/PVDF dual-layer hollow fiber ultrafiltration membrane. *J. Membr. Sci.* **506**, 1–10 (2016).
- Shevate, R. et al. Polydopamine/cysteine surface modified isoporous membranes with self-cleaning properties. *J. Membr.* Sci. 529, 185–194 (2017).
- Phillip, W. A. et al. Tuning structure and properties of graded triblock terpolymer-based mesoporous and hybrid films. Nano Lett. 11, 2892–2900 (2011).
- 31. Deen, W. M. Hindered transport of large molecules in liquid-filled pores. *AIChE J.* **33**, 1409–1425 (1987).
- 32. Zeman, L. & Wales, M. in *Synthetic Membranes* Vol. II (ed. Turbak, A. F.) 411–434 (American Chemical Society, 1981).
- Striemer, C. C. et al. Charge- and size-based separation of macromolecules using ultrathin silicon membranes. *Nature* 445, 749–753 (2007).
- Ren, J. et al. Post-directed-self-assembly membrane fabrication for in situ analysis of block copolymer structures. *Nanotechnology* 27, 435303 (2016).
- 35. Peng, Q. et al. Effect of nanostructured domains in self-assembled block copolymer films on sequential infiltration synthesis. *Langmuir* **33**, 13214–13223 (2017).
- 36. Tseng, Y.-C. et al. Enhanced block copolymer lithography using sequential infiltration synthesis. *J. Phys. Chem.* C **115**, 17725–17729 (2011).
- Shao, J. & Baltus, R. E. Hindered diffusion of dextran and polyethylene glycol in porous membranes. AIChE J. 46, 1149–1156 (2000).
- 38. Zydney, A. L. & Xenopoulos, A. Improving dextran tests for ultrafiltration membranes: effect of device format. *J. Membr. Sci.* **291**, 180–190 (2007).
- 39. Phillip, W. A. et al. Diffusion and flow across nanoporous polydicyclopentadiene-based membranes. ACS Appl. Mater. Interfaces 1, 472–480 (2009).

- Mehta, A. & Zydney, A. L. Permeability and selectivity analysis for ultrafiltration membranes. J. Membr. Sci. 249, 245–249 (2005).
- Dhanasekaran, J. & Koch, D. L. Model for the radial distribution function of polydisperse inertial spheres settling in homogeneous, isotropic turbulence. *Phys. Rev. Fluids* 7, 104602 (2022).
- Peng, Q. et al. Nanoscopic patterned materials with tunable dimensions via atomic layer deposition on block copolymers. Adv. Mater. 22, 5129–5133 (2010).
- Zaluzec, N. First light on the Argonne PicoProbe and the X-Ray perimeter array detector (XPAD). *Microsc. Microanal.* 27, 2070–2074 (2021).
- Gao, F. et al. Exploring the limits of size-selectivity in nanoscale solute separations. *Figshare* https://doi.org/10.6084/ m9.figshare.24773811.v1 (2023).

# **Acknowledgements**

This work was supported as part of the Advanced Materials for Energy-Water Systems (AMEWS) Center, an Energy Frontier Research Center funded by the US Department of Energy, Office of Science, Basic Energy Sciences at Argonne National Laboratory under contract DE-ACO2-06CH11357. We would like to thank P. Griffin at the Soft Matter Characterization Facility of the University of Chicago for the helpful discussion of GPC analysis. We would also like to thank S. Yim and J. Dhanasekaran for their support of the nanofabrication process, dextran sample GPC measurements and solute transport discussion, respectively.

### **Author contributions**

S.B.D. and P.F.N. conceived the idea and designed the research. F.G., W.C., J.G.E. and R.Z.W. conducted the experiments and analysed the experimental results. R.D. performed GPC. N.J.Z. executed TEM. F.G., W.C. and J.G.E. contributed to drafting and revising the paper. S.B.D.

and P.F.N contributed to proofreading and revising the paper. S.B.D. and P.F.N. supervised the project and contributed to the funding acquisition.

# **Competing interests**

The authors declare no competing interests.

#### Additional information

**Supplementary information** The online version contains supplementary material available at https://doi.org/10.1038/s44221-024-00252-3.

**Correspondence and requests for materials** should be addressed to Seth B. Darling.

**Peer review information** *Nature Water* thanks Chanhee Boo, Anthony Straub and the other, anonymous, reviewer(s) for their contribution to the peer review of this work.

**Reprints and permissions information** is available at www.nature.com/reprints.

**Publisher's note** Springer Nature remains neutral with regard to jurisdictional claims in published maps and institutional affiliations.

Springer Nature or its licensor (e.g. a society or other partner) holds exclusive rights to this article under a publishing agreement with the author(s) or other rightsholder(s); author self-archiving of the accepted manuscript version of this article is solely governed by the terms of such publishing agreement and applicable law.

© UChicago Argonne, LLC, Operator of Argonne National Laboratory and Ruilin Dong, Paul F. Nealey, under exclusive licence to Springer Nature Limited 2024